

# Università degli Studi di Napoli Federico II



SCUOLA POLITECNICA E DELLE SCIENZE DI BASE

DIPARTIMENTO DI INGEGNERIA ELETTRICA E DELLE  
TECNOLOGIE DELL'INFORMAZIONE

CORSO DI LAUREA MAGISTRALE IN INGEGNERIA DELL'AUTOMAZIONE E  
ROBOTICA

FIELD AND SERVICE ROBOTICS

## HOMEWORK 4

**Docente:**  
PROF. FABIO RUGGIERO

**Studente:**  
DARIO BARBATO P38000243

## GITHUB

[https://github.com/Dario54321/FIELD\\_HOMEWORK\\_4.git](https://github.com/Dario54321/FIELD_HOMEWORK_4.git)

ANNO ACCADEMICO 2024/2025

# Contents

<b>1</b>	<b>The Buoyancy Effect in Underwater Robotics</b>	<b>1</b>
<b>2</b>	<b>Concept Validation</b>	<b>2</b>
<b>3</b>	<b>Quadruped Simulation</b>	<b>3</b>
3.1	qpSWIFT . . . . .	4
3.2	GAIT . . . . .	4
3.3	TROT . . . . .	5
3.4	BOUND . . . . .	6
3.5	PACING . . . . .	7
3.6	GALLOP . . . . .	8
3.7	TROT RUN . . . . .	8
3.8	CRAWL . . . . .	10
<b>4</b>	<b>Rimless Wheel</b>	<b>10</b>

# The Buoyancy Effect in Underwater Robotics

When a rigid body is submerged in a fluid, its dynamics are influenced by two fundamental forces: the gravitational force and the buoyancy force. Buoyancy is defined as a hydrostatic effect, meaning it is independent of the relative motion between the body and the fluid. Its magnitude is given by the expression:

$$b = \rho \Delta \|g\| \quad (1.1)$$

where  $\rho$  is the fluid density,  $\Delta$  is the volume of the submerged body, and  $\|\bar{g}\|$  is the magnitude of the gravitational acceleration. This force acts upwards through a specific point known as the center of buoyancy ( $\mathbf{r}_b^b$ ). In the domain of underwater robotics, the buoyancy effect is a critical consideration that must be explicitly included in the dynamic model. This necessity arises because the density of water is comparable to the density of the robot itself, a principle also highlighted in the discussion of added mass effects. Consequently, the buoyant force is of a significant magnitude relative to the robot's weight,  $w = m\|g\|$ .

The interaction between the gravitational force, acting at the center of mass ( $\mathbf{r}_c^b$ ), and the buoyant force, acting at the center of buoyancy, is formally captured by the restoring wrench,  $\mathbf{g}_{rb}^b$ , expressed in the body-fixed frame:

$$\mathbf{g}_{rb}^b = - \begin{bmatrix} \mathbf{f}_g^b + \mathbf{f}_b^b \\ S(\mathbf{r}_c^b)\mathbf{f}_g^b + S(\mathbf{r}_b^b)\mathbf{f}_b^b \end{bmatrix} \in \mathbb{R}^6 \quad (1.2)$$

This wrench represents the combined forces and torques that act on the vehicle. These are defined as restoring forces and are a major concern in control design for two primary reasons:

1. They are persistent dynamic terms, meaning they exert a non-null contribution on the system even when the vehicle is stationary.
2. Any spatial misalignment between the center of mass and the center of buoyancy results in a non-zero torque component in the wrench ( $S(\mathbf{r}_c^b)\mathbf{f}_g^b + S(\mathbf{r}_b^b)\mathbf{f}_b^b \neq \mathbf{0}$ ). For large vehicles, even a small displacement between these two points can generate significant torques, which in turn require large control efforts from the thrusters to compensate.

Therefore, due to its direct and significant impact on both the translational and rotational dynamics, the buoyancy effect is an indispensable component of the complete dynamic model for an Unmanned Underwater Vehicle (UUV).

## Neglect in Aerial Robotics

Conversely, the buoyancy effect is justifiably neglected in the dynamic modeling of aerial robots. While air is technically a fluid, its density is vastly lower than that of the solid materials comprising a typical robot's mechanical system.

Following the same reasoning applied to the consideration of added mass, the buoyant force exerted by the displaced air is many orders of magnitude smaller than the gravitational force acting on the robot. Because this force is so minimal, its contribution to the overall dynamics is negligible compared to the dominant forces of gravity and aerodynamics. Any torque it might generate would be insignificant relative to the moments produced by the propulsion system. As a result, it is standard and sound engineering practice to omit the buoyancy term from the dynamic equations of aerial systems, as it does not contribute meaningfully to their behavior, stability, or control.

# Concept Validation

a. **The added mass effect considers an additional load to the structure. FALSE.** The added mass effect is a purely dynamic phenomenon, not a static load. It represents the inertial reaction force from the surrounding fluid that must be accelerated as the body moves. This effect increases the body's *apparent inertia*, not its physical mass. In the dynamic model, this is captured by an added mass matrix,  $M_A$ , which is a function of the body's geometry, and an associated Coriolis term,  $C_A$ . **Crucially, this force is proportional to the body's acceleration, distinguishing it from a static load which is constant.**

b. **The added mass effect is considered in underwater robotics since the density of the underwater robot is comparable to the density of the water. TRUE.** The significance of the added mass effect is dictated by the ratio of fluid density to body density. In underwater applications, the density of water is comparable to that of the vehicle, making the inertia of the accelerated fluid non-negligible. This requires its inclusion in the dynamic model for accuracy. In contrast, for aerial robots, the density of air is several orders of magnitude lower than the robot's structure, rendering the effect insignificant.

c. **The damping effect helps in the stability analysis. TRUE.** Damping, caused by fluid viscosity, introduces dissipative forces that oppose motion and remove energy from the system. These effects are modeled via a positive definite damping matrix,  $D_{RB}$ . In stability analysis, such as with Lyapunov methods, this guaranteed energy dissipation is crucial for proving that system trajectories will converge to a stable equilibrium by suppressing oscillations. **This makes damping a key stabilizing property of the system's natural dynamics.**

d. **The Ocean current is usually considered as constant, and it is better to refer it with respect to the body frame. FALSE.** The statement is flawed in both its assumption and its choice of reference frame. Firstly, assuming the ocean current is constant is a common modeling simplification for what is, in reality, a dynamic phenomenon. Secondly, and more critically, this assumption of constancy is only valid in the **world (inertial) frame**, as the current is an external environmental disturbance. Defining the current in the rotating body frame would be a fundamental error, as it would **falsely attribute changes in the current's vector to the environment instead of the robot's own motion**. The correct procedure is to define the constant current vector in the world frame and then compute the robot's relative velocity, **which is subsequently used to determine the hydrodynamic forces in the body-frame equations.**

# Quadruped Simulation

This exercise focuses on the simulation and analysis of a quadruped robot using the provided Matlab files within the `quadruped_simulation.zip` package. The main executable file, `MAIN.m`, runs the simulation and generates animations alongside plots that illustrate the robot's position, velocity, and the vertical component of ground reaction forces. The objective is to implement a quadratic programming (QP) function using the `qpSWIFT` solver and to explore how varying gait patterns, desired velocities, and physical parameters such as friction and mass affect the robot's behavior. Through execution and analysis of these simulations, the exercise aims to deepen understanding of robot locomotion dynamics and control strategies.

## 3.1 qpSWIFT

The `qpSWIFT` solver is an interior-point-based QP solver, efficient for problems with linear equality and inequality constraints. In the quadruped simulation, the QP problem is formulated as:

$$\min_x \frac{1}{2}x^\top Hx + g^\top x, \quad \text{s.t. } A_{ineq}x \leq b_{ineq}, \quad A_{eq}x \leq b_{eq},$$

where  $H, g, A_{ineq}, b_{ineq}, A_{eq}, b_{eq}$  are obtained from the function `fcn_get_QP_form_eta`. Implementation steps:

- convert all matrices to `sparse` format;
- call the solver using: `[zval, basic_info, adv_info] = qpSWIFT(H, g, Aeq, beq, Aineq, bineq);`
- store the solution in `zval` for use in subsequent control and simulation steps.

Using `qpSWIFT` allows efficient resolution of complex QP problems, which are crucial for dynamic motion planning and control of the quadruped robot under physical constraints such as friction and force limits.

## 3.2 GAIT

The default physical parameters define the basic dynamics of the quadruped robot used in simulation. The robot has a mass of 5.5 kg and a diagonal inertia matrix  $\mathbf{J} = \text{diag}(0.026, 0.112, 0.075) \text{ kg}\cdot\text{m}^2$ , representing its rotational resistance around the principal axes. The gravitational acceleration is set to  $9.81 \text{ m/s}^2$ , and the coefficient of friction between the feet and the ground is  $\mu = 1$ , ensuring stable contact. The center of mass (COM) is nominally positioned at a height of 0.2 m. These values serve as a baseline for analyzing the robot's locomotion under different gaits and parameter variations.

**Gaits Description.** In the quadruped simulation, different gaits represent specific leg coordination strategies for locomotion. The gait parameter in the code selects one of the following predefined patterns:

- **0 - Trot:** A symmetric gait where diagonal pairs of legs (front-left and rear-right, front-right and rear-left) move together. It is efficient and commonly used at moderate speeds.
- **1 - Bound:** A faster gait where both front legs move together, followed by both rear legs. This gait features a flight phase and is typical in agile movements, like those of a rabbit.

- **2 - Pacing:** A lateral gait in which legs on the same side (left or right) move in unison. This gait is less stable but observed in some animals like camels and giraffes.
- **3 - Gallop:** A high-speed, asymmetrical gait involving a sequence where front and hind legs strike the ground at different times. It includes an aerial phase and resembles the gait of running dogs or horses.
- **4 - Trot Run:** A variation of the trot adapted for higher speeds, typically with shorter stance phases and potential brief flight phases. It combines symmetry with dynamic movement.
- **5 - Crawl:** A slow, statically stable gait where only one leg moves at a time while the other three support the body. It maximizes stability and is suitable for rough terrains or low-speed maneuvers.

### 3.3 TROT

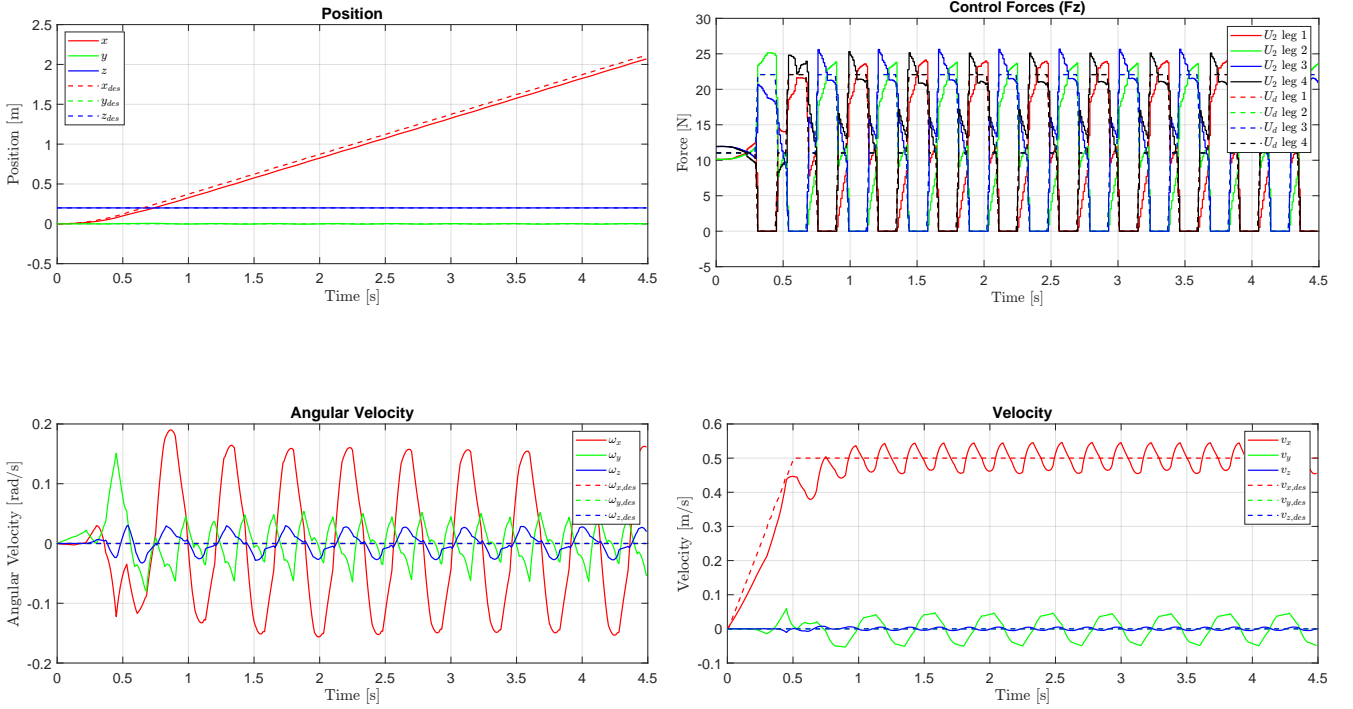


Figure 3.1: Position, Force , Angular velocity e Velocity for Trot Gait

These plots represent the robot's performance under the default parameter settings, executing a standard trotting gait with a desired forward velocity of 0.5 m/s and an acceleration of 1 m/s<sup>2</sup>. This scenario serves as a baseline to evaluate the fundamental stability and tracking capabilities of the controller.

The velocity tracking in this case is highly effective. The robot's forward velocity,  $v_x$ , quickly reaches the desired 0.5 m/s and maintains it with only minor oscillations around the target value. These small ripples are inherent to the discrete push-off phases of the trotting gait. Consequently, the position tracking is excellent. The actual position,  $x$ , follows the desired trajectory,  $x_{des}$ , with negligible error, demonstrating the controller's ability to achieve precise motion tracking at moderate speeds. Lateral and vertical stability are also maintained effectively, with  $y$  and  $z$  positions held nearly constant.

The angular velocity plot highlights the robot's stability. Unlike the aggressive, commanded pitching seen in the high-speed case, here the desired angular velocities are all zero. The controller's primary goal is to keep the body perfectly level. The small oscillations observed in roll ( $\omega_x$ ) and pitch ( $\omega_y$ ), within a tight band of approximately  $\pm 0.15$  rad/s, are minor disturbances caused by the shifting of weight between leg pairs. The controller's ability to quickly suppress these disturbances demonstrates robust posture stabilization.

The vertical ground reaction forces ( $F_z$ ) are significantly lower and more controlled than in the high-speed scenario. Peak forces are approximately 25 N per leg. This value is consistent with the physical requirements: to support the robot's total weight of approximately 54 N, each of the two stance legs must provide about 27 N on average. The forces are just slightly above this value to generate the gentle forward propulsion needed. The excellent tracking between the desired forces ( $U_d$ ) and the actual forces ( $U_2$ ) confirms that the QP solver is generating accurate and feasible commands that are well within the system's capabilities.

### 3.4 BOUND

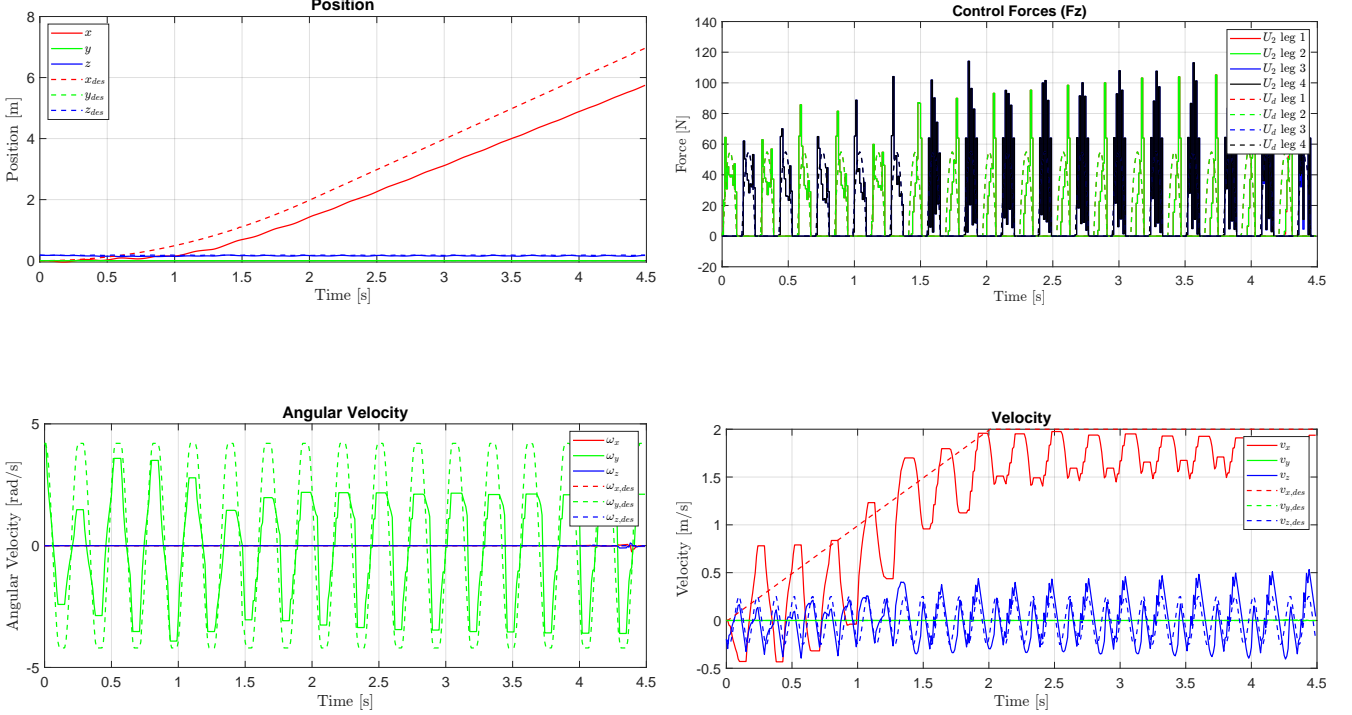


Figure 3.2: Position, Force , Angular velocity e Velocity for Bound Gait

To evaluate the controller's performance under highly dynamic conditions, we modified the default simulation parameters. Specifically, the desired forward velocity was increased from 0.5 m/s to 1.5 m/s, and the acceleration was set to 3 m/s<sup>2</sup>. At the same time, the nominal center of mass (COM) height was reduced to 0.18 m, and the friction coefficient was lowered to 0.9. These changes resulted in a more physically demanding scenario, highlighting the importance of precise and agile control strategies.

The robot successfully reaches the target forward velocity of 1.5m/s. However, the longitudinal velocity ( $v_x$ ) shows significant oscillations, which are characteristic of a dynamic bound gait. These oscillations are a necessary consequence of the alternating flight and stance phases. As a result, the forward position ( $x$ ) exhibits a growing tracking error, with the robot lagging slightly behind the desired trajectory. In contrast, the lateral ( $y$ ) and vertical ( $z$ ) positions remain well controlled, highlighting the controller's prioritization of posture stability over perfect tracking performance in high-speed scenarios.

The angular velocity plot reveals large oscillations in the pitch rate ( $\omega_y$ ). These are not signs of instability but rather part of a deliberate control strategy. The actual pitch angular velocity closely follows the desired trajectory ( $\omega_{y,des}$ ), indicating that the controller is actively using pitching motions to redistribute inertia and maintain dynamic balance. This "leaning" behavior is essential for compensating the forward momentum and supporting aerial phases.

The vertical ground reaction forces ( $F_z$ ) show peaks exceeding 110N, which is more than twice the robot's weight (approximately 54N). Such forces are necessary to support the robot during two-legged stance phases and to generate strong propulsion. The alternating force patterns reflect the bounding gait and demonstrate that the QP solver successfully computes feasible force

distributions that satisfy the physical constraints, even under reduced friction conditions.

### 3.5 PACING

This analysis evaluates the controller's performance with a pacing gait, a locomotion pattern known for its lateral instability. The robot's parameters were modified by reducing the mass to 4.5 kg (from the original 5.5 kg) and increasing the friction coefficient to 1.6. The desired forward velocity was set to 0.8 m/s.

The key challenge of the pacing gait—where legs on the same side move together—is immediately evident in the velocity and angular velocity plots. To counteract the inherent tendency to tip laterally, the controller actively induces lateral motion. The lateral velocity  $v_y$  (green) shows large, periodic oscillations of approximately  $\pm 0.4$  m/s, indicating that the robot is deliberately shifting its center of mass from side to side to maintain balance. This behavior is mirrored in the roll angular velocity  $\omega_x$  (red), which exhibits the largest oscillations among all angular components. These motions represent the controller's continuous effort to stabilize the robot in the lateral plane.

In contrast, the forward velocity  $v_x$  accurately tracks the desired 0.8 m/s, demonstrating the controller's ability to balance stabilization with forward propulsion.

The position plot further confirms this strategy. While the forward position  $x$  tracks the reference trajectory closely, the lateral position  $y$  exhibits oscillations around zero, reflecting the lateral sway characteristic of pacing gaits.

The control forces plot reveals the expected gait pattern, with legs on the same side (e.g., 1 and 3) producing ground reaction forces simultaneously. The peak vertical forces reach approximately 35 N, which aligns with the requirements of supporting the reduced body weight (about 44 N) while also generating forward thrust. The high friction coefficient  $\mu = 1.6$  provides the controller with a substantial margin to generate these forces effectively without risking slippage.

In conclusion, the simulation demonstrates that the controller can successfully execute the challenging and inherently unstable pacing gait by adopting an active, oscillatory stabilization strategy, particularly in the roll axis, made feasible by the favorable friction conditions.

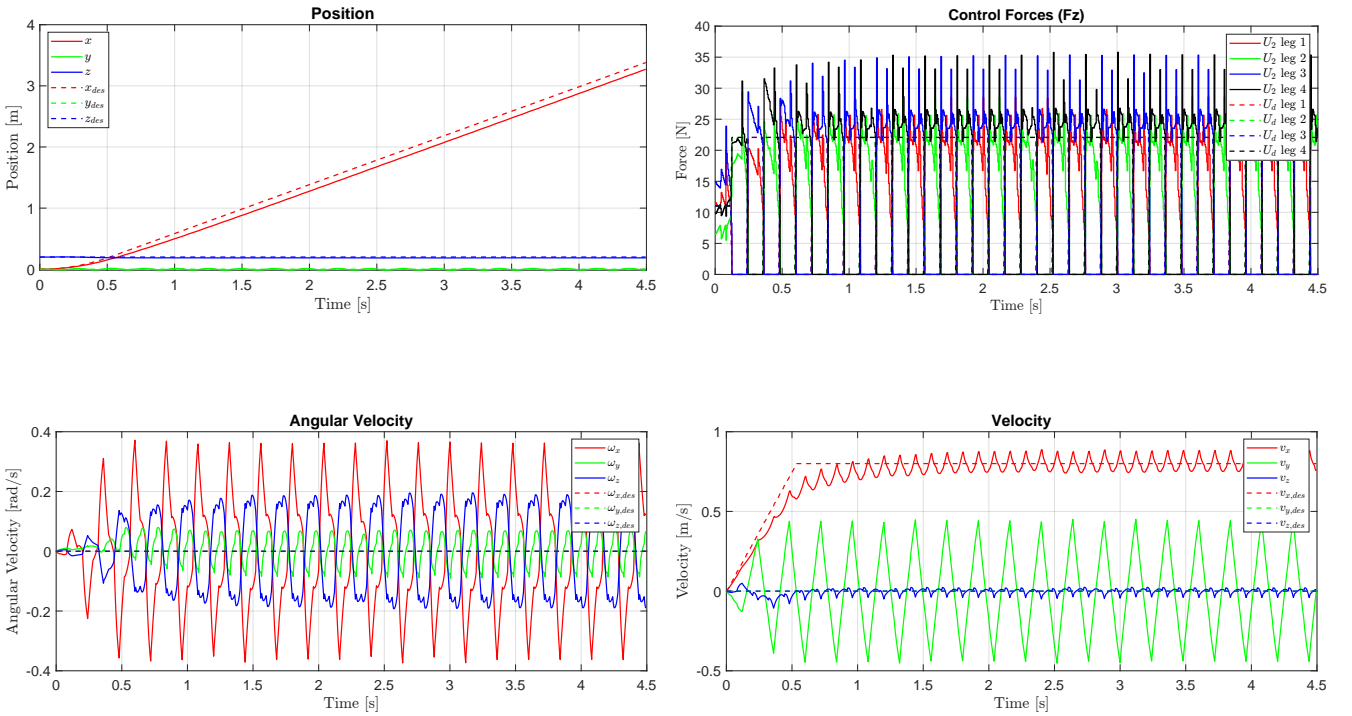


Figure 3.3: Position, Force , Angular velocity e Velocity for Pacing Gait



### 3.6 GALLOP

This analysis examines the robot's performance while executing a galloping gait, a dynamic and asymmetric locomotion pattern characterized by a leading leg pair (either front or rear) and a flight phase during which all feet are off the ground. The robot's mass was reduced to 4.3 kg, and the desired forward velocity was set to 0.5 m/s. A relatively high friction coefficient of 1.2 was used to allow for sufficient traction during rapid push-off phases.

The velocity plot reveals the distinctive signature of galloping. The forward velocity  $v_x$  exhibits large, periodic oscillations ranging from approximately  $-0.4$  m/s to over  $1.0$  m/s, despite the constant desired value of 0.5 m/s. These fluctuations reflect the alternating phases of rapid acceleration during leg extension and deceleration during the aerial phase. As a result, the average forward velocity tends to fall below the desired value, leading to a noticeable and growing tracking error in the forward position  $x$ .

The angular velocity plot emphasizes the dominant role of pitching in galloping. The pitch angular velocity  $\omega_y$  shows large oscillations reaching nearly  $\pm 0.7$  rad/s. These are not signs of instability but intentional control actions used to generate propulsion: the robot dynamically rocks forward and backward to achieve forward thrust. The roll ( $\omega_x$ ) and yaw ( $\omega_z$ ) components also show significant activity, likely due to asymmetries in contact and motion. However, the robot remains stable, indicating that the controller is effectively managing the resulting disturbances.

The ground reaction forces confirm the galloping pattern. The rear legs produce strong impulses, followed by the front legs, creating a periodic force profile. Peak vertical forces exceed 70 N, well above the static weight of approximately 42 N. These high forces are necessary to lift the entire body off the ground and sustain the flight phase. The elevated friction coefficient  $\mu = 1.2$  ensures that the necessary horizontal and vertical forces can be generated without slippage.

In conclusion, the simulation demonstrates that the controller is capable of generating a stable galloping gait. This is achieved through large, coordinated pitching motions and high-magnitude impulsive ground forces. While this mode sacrifices precise velocity and position tracking due to its ballistic nature, it succeeds in maintaining dynamic balance and realistic gallop dynamics.

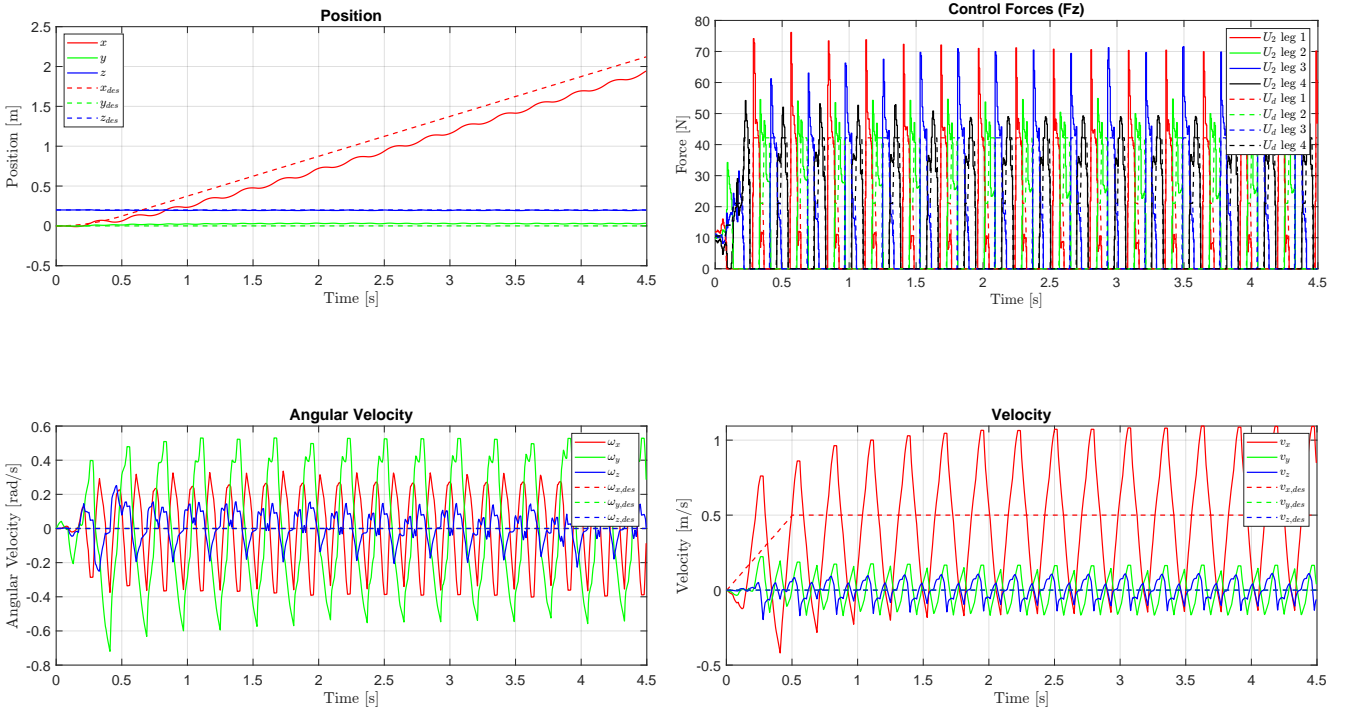


Figure 3.4: Position, Force , Angular velocity e Velocity for Pacing Gait

### 3.7 TROT RUN

This analysis evaluates the robot's performance using a trotting-run gait, a faster and more dynamic variant of the standard trot. This gait includes a brief flight phase during which all legs are

off the ground. The robot's mass was set to 5.0 kg, with an increased nominal center of mass height of 0.22 m and a reduced friction coefficient of 0.75. The desired forward velocity was maintained at 0.5 m/s to isolate the effects of gait dynamics from speed variation.

The velocity plots demonstrate excellent forward tracking. The longitudinal velocity  $v_x$  rapidly reaches the target of 0.5 m/s and maintains it with only minor oscillations, confirming stable and effective propulsion. However, small but consistent deviations from zero are observed in the lateral ( $v_y$ ) and vertical ( $v_z$ ) velocity components. These reflect the dynamic nature of the gait and result in slight tracking errors in the lateral and vertical positions. The forward position  $x$  tracks the reference well, with only a minor lag accumulating over time.

The angular velocity plot confirms the system's stability. All desired angular velocities are set to zero, and the controller effectively suppresses disturbances in roll ( $\omega_x$ ), pitch ( $\omega_y$ ), and yaw ( $\omega_z$ ). The observed oscillations are low in magnitude (approximately  $\pm 0.2$  rad/s) and periodic, arising from the alternating leg contacts and the presence of flight phases. Their bounded nature indicates robust posture stabilization even during dynamic transitions.

The control forces provide further insight into the gait execution. The trotting-run is marked by the activation of diagonal leg pairs in sequence, and the presence of "flight phases" is evident from brief intervals where all vertical ground reaction forces drop to zero (e.g., at  $t = 0.7$  s and  $t = 0.95$  s). To enable liftoff, the robot must generate vertical forces significantly exceeding its static weight (approximately 49 N). The force peaks surpass 60 N, providing the necessary impulse while still respecting the friction constraints imposed by  $\mu = 0.75$ .

In conclusion, the controller successfully executes a dynamic and stable trotting-run gait. It maintains precise velocity tracking and robust orientation control through well-timed, high-magnitude control forces, effectively compensating for the reduced friction and elevated COM height.

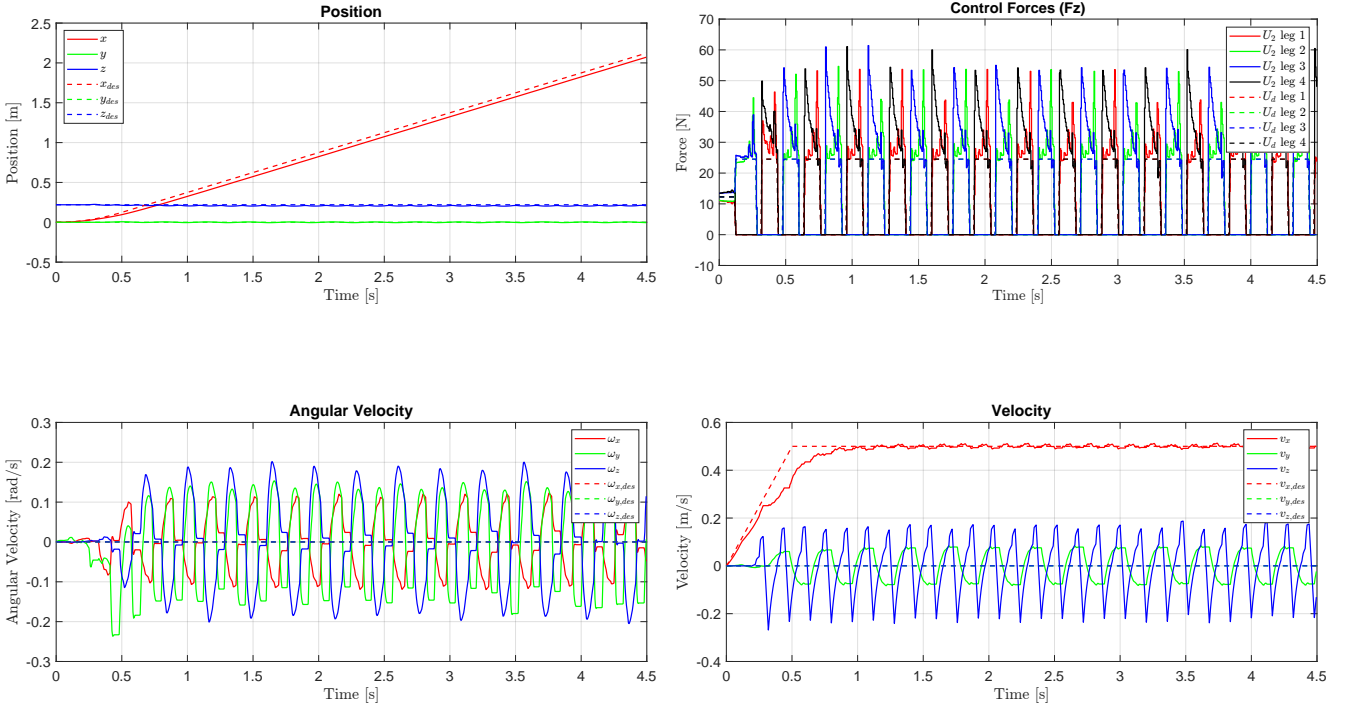


Figure 3.5: Position, Force , Angular velocity e Velocity for Trot Run Gait

### 3.8 CRAWL

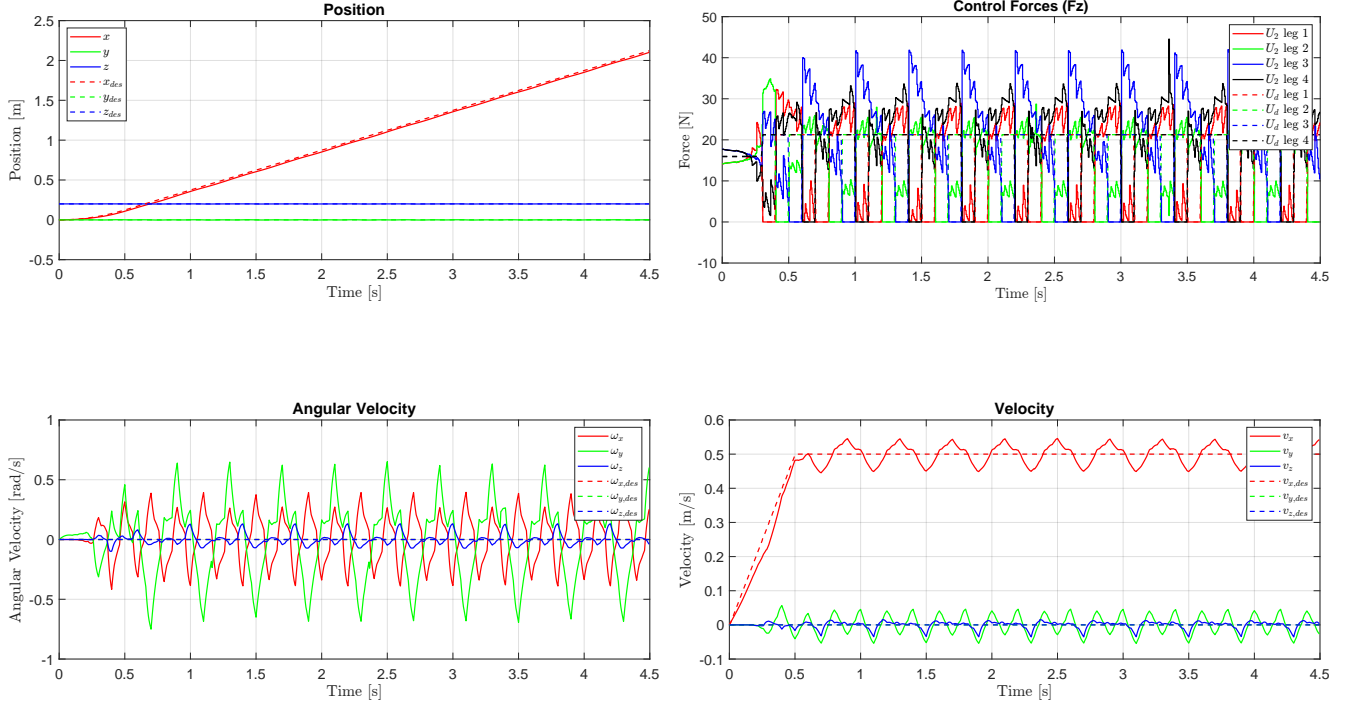


Figure 3.6: Position, Force , Angular velocity e Velocity for Pacing Gait

This simulation evaluates the crawling gait, which is characterized by its static stability—at least three legs are always in contact with the ground. To assess the controller’s performance under heavier payloads, the robot’s mass was increased to 6.5 kg, and the friction coefficient was set to a high value of 1.5. This configuration provides a large stability margin, enabling careful observation of control behavior in quasi-static conditions.

The position and velocity plots reveal the primary strength of the crawling gait: excellent tracking performance. The forward position  $x$  and velocity  $v_x$  closely follow their desired trajectories with negligible tracking error and minimal oscillations. This smooth motion results from the continuous three-point support, which eliminates the dynamic bounding phases typical of faster gaits and allows the center of mass to be moved with greater precision.

The control force plot clearly shows the expected crawling pattern. At any given time, three legs are in stance while one is in swing phase, indicated by a ground reaction force near zero. The robot’s total weight is approximately 63.8 N ( $6.5 \text{ kg} \times 9.81 \text{ m/s}^2$ ), meaning each stance leg supports roughly 21 N. This matches the actual forces computed by the controller, confirming proper load distribution. The high friction coefficient of  $\mu = 1.5$  provides ample grip, ensuring that the robot remains stable and avoids slippage throughout the motion.

Interestingly, the angular velocity plot reveals noticeable oscillations in roll ( $\omega_x$ ), pitch ( $\omega_y$ ), and yaw ( $\omega_z$ ). These are not indicators of instability, but rather natural consequences of the asymmetry introduced when lifting a single leg. Each swing phase generates unbalanced moments that perturb the body orientation. The controller actively compensates for these multi-axis disturbances to maintain a level posture. Despite these angular corrections, the robot’s global trajectory remains smooth and accurate.

In conclusion, the crawling gait offers superior positional tracking and robustness, especially under heavy loading. Its inherent stability allows precise motion, though it requires constant orientation corrections due to the asymmetric nature of single-leg lift-offs. This makes the gait particularly suitable for tasks involving high precision or transport of heavier payloads.

# Rimless Wheel

This exercise involves the analysis of the passive dynamics of a rimless wheel using the provided MATLAB script `rimless_wheel.m`. The rimless wheel is a simplified model often used to study legged locomotion and stability of walking gaits. The simulation enables the observation of the system's behavior under different initial conditions and parameter settings.

The task is divided into two main parts. First, the effect of varying the initial angular velocity (both positive and negative) is explored by analyzing the state trajectories and phase portraits, with a focus on identifying equilibrium points, limit cycles, and their basins of attraction. Second, key physical parameters such as leg length, inter-leg angle, and slope inclination are modified to investigate how they influence the existence and stability of equilibrium behaviors. The analysis aims to develop a deeper understanding of the system's nonlinear dynamics and the conditions under which stable periodic motion arises.

## Simulation and Analysis

The rimless wheel is a canonical model for passive dynamic walking. The system consists of a point mass at the hip and rigid, massless legs, walking down a slope of angle  $\gamma$ . Its hybrid dynamics alternate between a continuous swing phase and a discrete, energy-dissipating impact event.

During the swing phase, the system behaves as an inverted pendulum, governed by:

$$\ddot{\theta} = \frac{g}{l} \sin(\theta).$$

Impact occurs when the leg angle satisfies the condition  $\theta = \gamma \pm \alpha$ . The subsequent inelastic collision is modeled by the impact map:

$$\dot{\theta}^+ = \dot{\theta}^- \cos(2\alpha).$$

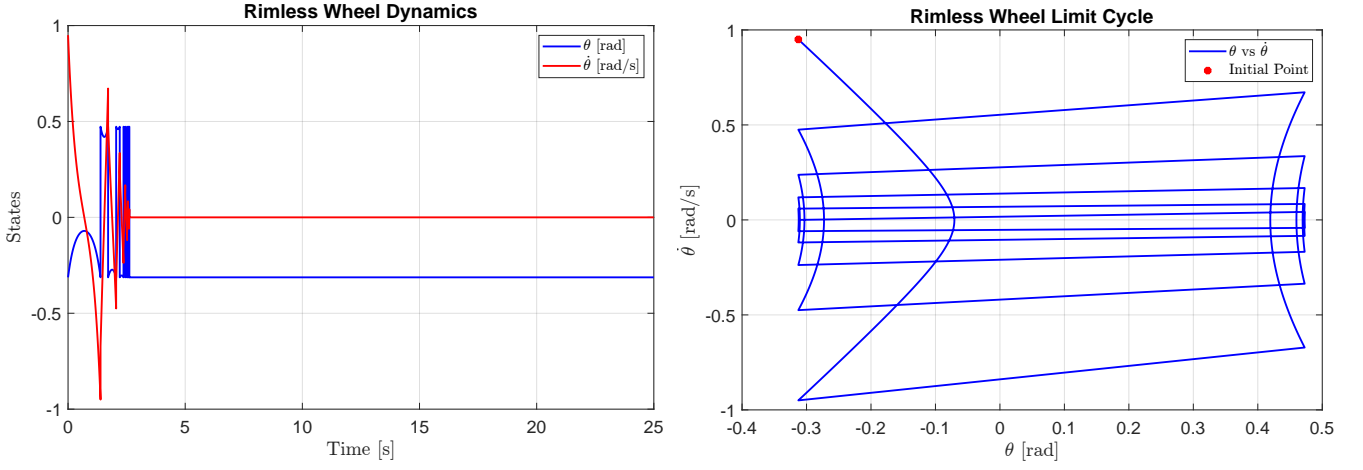
A critical condition for initiating locomotion is that the initial kinetic energy must be sufficient to vault the center of mass over the stance foot. This defines a minimum velocity threshold,  $\omega_1$ :

$$\omega_1 = \sqrt{\frac{2g}{l} (1 - \cos(\gamma - \alpha))}.$$

For the simulation parameters ( $\gamma = 0.08$  rad,  $\alpha = \pi/8$  rad), this threshold is  $\omega_1 \approx 0.9754$  rad/s. An analysis of the provided `rimless_wheel.m` script revealed that its default initial velocity of  $\dot{\theta}_0 = 0.95$  rad/s was insufficient to sustain motion.

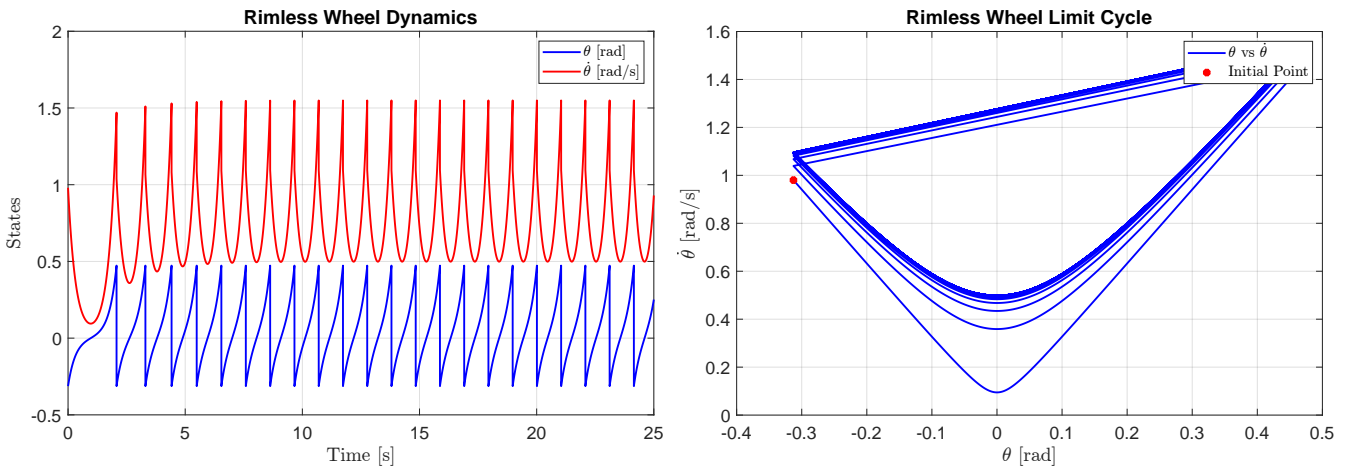
Simulations were conducted to analyze the system's behavior relative to this threshold.

- **For  $\dot{\theta}_0 < \omega_1$  (e.g., the default 0.95 rad/s), the system fails to complete the first step. It rocks back and forth, quickly losing its remaining energy and settling at the **zero-velocity equilibrium point**.**



This simulation was run with an initial angular velocity of  $\dot{\theta}_0 = 0.95$  rad/s. The system completes one step (the first impact is visible as a drop in  $\dot{\theta}$ ), but the post-impact velocity is insufficient to initiate another. As a result, it oscillates with decreasing amplitude and quickly comes to rest. Both  $\theta$  and  $\dot{\theta}$  converge to constant values:  $\dot{\theta} \rightarrow 0$ , and  $\theta \rightarrow -0.31$  rad. The phase portrait confirms this behavior: the trajectory, starting from the initial point (red star), makes one large loop then spirals inward without forming a closed orbit, finally settling on the horizontal axis. This indicates convergence to a static equilibrium, not a limit cycle, so the plot title referring to a "limit cycle" is misleading. The final state is the static equilibrium  $(\theta, \dot{\theta}) \approx (-0.31, 0)$ , corresponding to the wheel resting on the slope with no motion. Although only one attractor is observed here, theory suggests the existence of another: a stable walking limit cycle. Its absence is due to insufficient initial energy. The critical angular velocity required to overcome gravity and enable walking is given by  $\omega_1 = \sqrt{2 \cdot \frac{g}{l}(1 - \cos(\gamma - \alpha))} \approx 0.9754$ . Since  $\dot{\theta}_0 = 0.95 < \omega_1$ , the system lacks sufficient energy to enter the limit cycle basin of attraction and instead converges to the static equilibrium. Therefore, this initial condition lies within the basin of attraction of the static equilibrium; initial conditions with  $\dot{\theta}_0 > \omega_1$  would lie in the basin of the walking limit cycle.

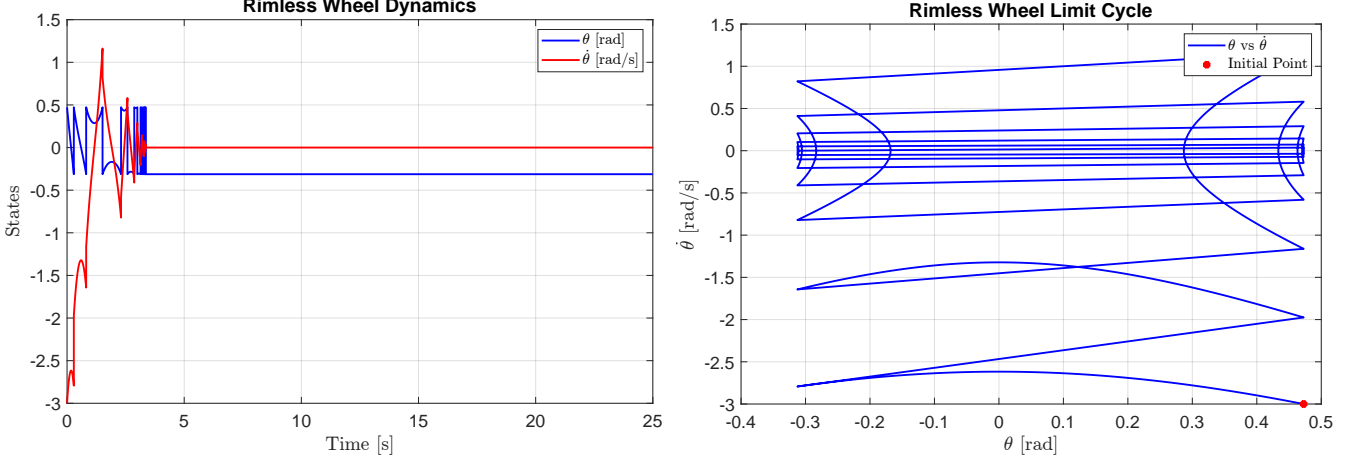
- **For  $\dot{\theta}_0 > \omega_1$**  (e.g., 0.98 rad/s), the system consistently converged to a **stable limit cycle**. The phase portrait shows all initial conditions in this region spiraling into a single closed orbit, representing a stable, periodic walking gait. This limit cycle acts as the system's primary attractor for forward motion.



This simulation uses an initial angular velocity of  $\dot{\theta}_0 = 0.98$  rad/s, which is slightly above the critical threshold  $\omega_1 \approx 0.9754$  rad/s. Unlike the  $\dot{\theta}_0 = 0.95$  case, here the system successfully enters a stable walking gait. The time history shows that after a brief transient phase, both  $\theta$  and  $\dot{\theta}$  settle into a periodic pattern. The velocity oscillates without approaching zero, and  $\theta$  follows a repeated sawtooth profile between  $\gamma + \alpha$  and  $\gamma - \alpha$ . The phase portrait shows convergence to a closed, isolated trajectory—a stable limit cycle—after a few steps. This demonstrates that

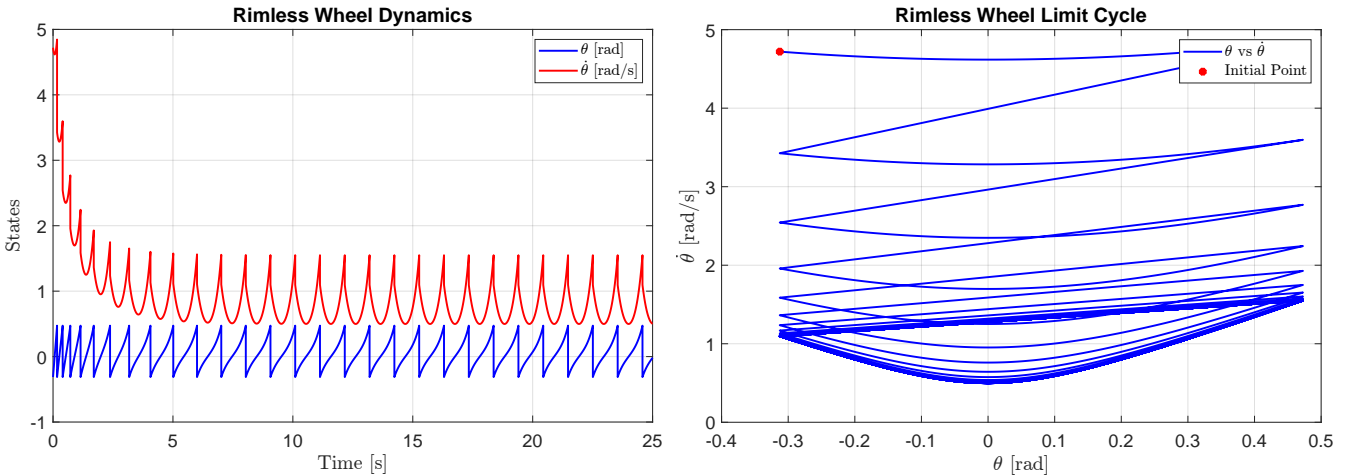
the system does not converge to a point equilibrium, but to a periodic orbit representing passive walking. Together with the previous result (static equilibrium at  $\dot{\theta}_0 = 0.95$ ), this confirms the system has two attractors: a static equilibrium and a walking limit cycle. The initial condition  $(\theta_0, \dot{\theta}_0) \approx (-0.31, 0.98)$  clearly lies in the basin of attraction of the limit cycle. The separatrix must lie between 0.95 and 0.98 rad/s, with  $\omega_1$  providing a good estimate of this boundary.

- For  $\dot{\theta}_0 < 0$  (e.g.,  $-3.0$  rad/s), the system moves backward uphill, reverses, but fails to sustain motion and ultimately converges to the **zero-velocity equilibrium point**.



This simulation explores the case  $\dot{\theta}_0 = -3.0$  rad/s, where the system is pushed backward uphill. Initially,  $\dot{\theta}$  is negative and  $\theta$  increases. Gravity slows the motion until the wheel reverses direction and starts rolling downhill. However, due to energy loss at impacts, the system cannot maintain forward motion. The time history shows that both  $\theta$  and  $\dot{\theta}$  decay, with the velocity converging to zero and the angle stabilizing near  $\theta \approx -0.31$  rad. The phase portrait starts in the bottom-right quadrant (positive  $\theta$ , negative  $\dot{\theta}$ ), arcs upward across  $\dot{\theta} = 0$ , and spirals inward to the static equilibrium point. This confirms that states with negative velocity still lie within the basin of attraction of the zero-velocity equilibrium. Thus, the static equilibrium basin includes both low-energy forward motion and backward motion scenarios.

- For  $\dot{\theta}_0 \gg \omega_1$  (e.g.,  $4.8$  rad/s), the system starts in a high-energy state, but dissipates excess energy over time and converges to the same **stable walking limit cycle**.



This simulation considers a high initial angular velocity,  $\dot{\theta}_0 = 4.8$  rad/s, far above the critical threshold  $\omega_1 \approx 0.9754$ . The time history shows that although large velocity drops occur at each impact due to energy loss, the system retains enough energy to sustain motion. Over several steps, the amplitude of oscillations in both  $\theta$  and  $\dot{\theta}$  gradually reduces, eventually settling into the same stable periodic gait observed in the lower-energy case ( $\dot{\theta}_0 = 0.98$ ).

The phase portrait confirms this convergence: starting from a high point on the  $\dot{\theta}$ -axis, the trajectory spirals inward through successive impacts, eventually locking into the same closed orbit—the limit cycle. This demonstrates that the walking gait is globally attractive for a wide range of initial conditions with  $\dot{\theta}_0 > \omega_1$ .

Therefore, the stable limit cycle not only withstands small perturbations but also attracts trajectories from high-energy states, illustrating the robustness of passive dynamic walking. This case reinforces the bistability of the system: initial conditions above the energy threshold converge to the walking cycle, while those below fall into the static equilibrium.

These results confirm the existence of two primary behaviors with distinct basins of attraction, fundamentally determined by whether the initial energy state is above or below the critical threshold required for one full step.

## Parameter Sensitivity Analysis

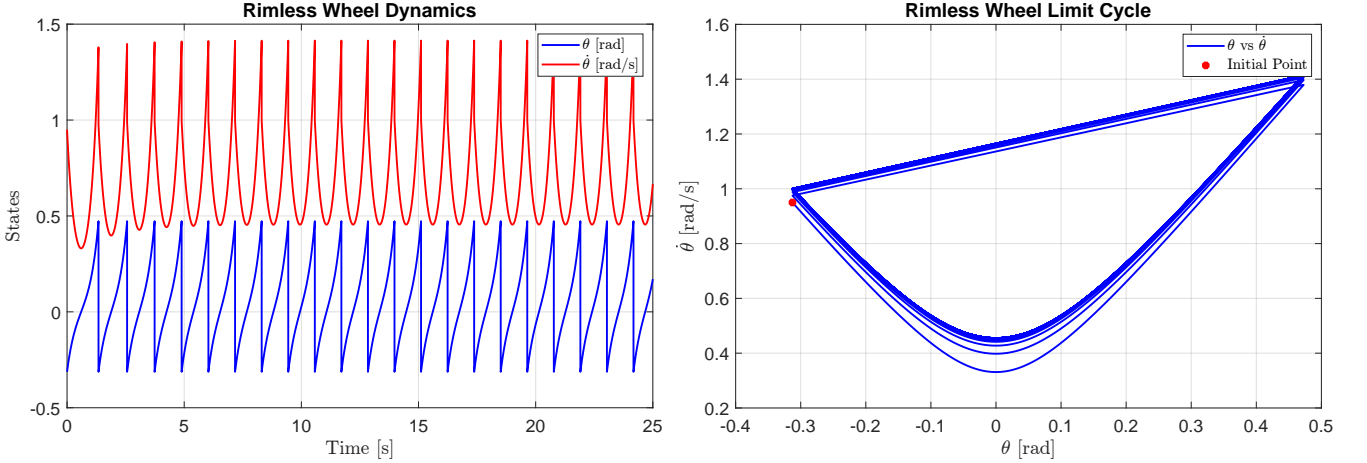
This section analyzes how changes in the rimless wheel’s physical parameters affect its ability to walk. Unlike previous cases, the initial angular velocity is fixed at a sub-critical value of  $\dot{\theta}_0 = 0.95$  rad/s, which previously led to static equilibrium.

We investigate whether modifying the leg length ( $l$ ), inter-leg angle ( $\alpha$ ), or slope angle ( $\gamma$ ) can lower the critical threshold

$$\omega_1 = \sqrt{\frac{2g}{l} (1 - \cos(\gamma - \alpha))},$$

making  $\dot{\theta}_0$  sufficient for walking. Each case explores how these changes affect system dynamics, especially the emergence and characteristics of limit cycles.

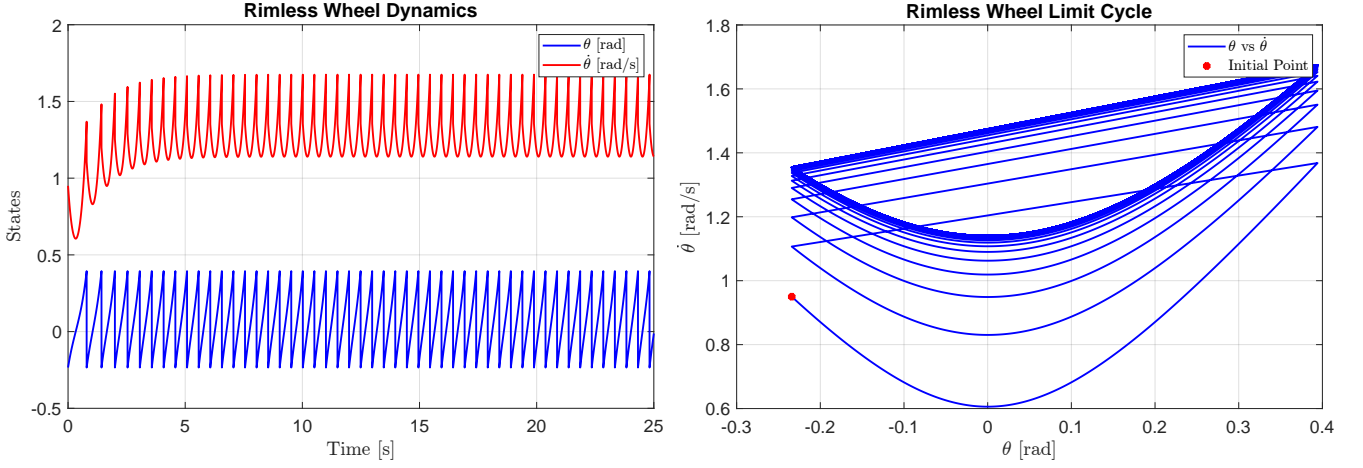
## Lenght



Increasing the leg length to  $l = 1.2$  m lowers the critical threshold to  $\omega_1 \approx 0.890$  rad/s, which is below the fixed  $\dot{\theta}_0 = 0.95$  rad/s. As predicted, the system now converges to a stable walking gait. The time history confirms periodic oscillations in  $\theta$  and  $\dot{\theta}$ , while the phase portrait shows convergence to a new limit cycle. This modification shifts the initial condition into the basin of attraction of the walking gait. Compared to the default case, the new cycle has a lower peak velocity (1.4 rad/s) and a longer period, reflecting a slower, steadier motion due to longer legs.

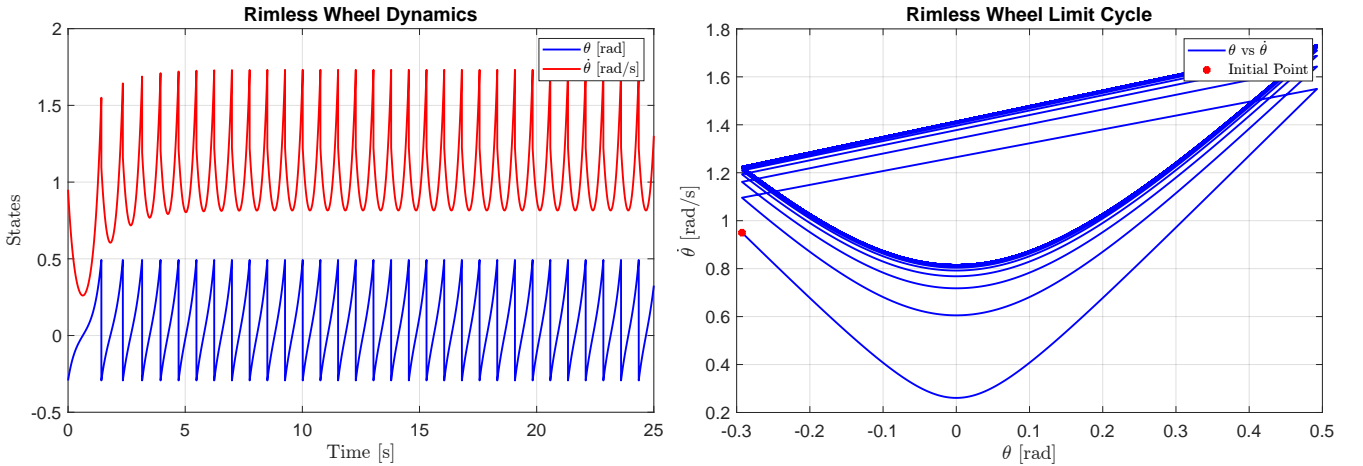


## Alpha



Reducing the inter-leg angle to  $\alpha = \pi/10$  lowers the critical threshold to  $\omega_1 \approx 0.732$  rad/s, enabling stable walking from the fixed  $\dot{\theta}_0 = 0.95$  rad/s. The system eventually converges to a periodic gait, though more slowly than in other cases. The phase portrait confirms convergence to a new limit cycle. This cycle features a narrower angular range (shorter steps) and a surprisingly higher peak velocity (1.7 rad/s), resulting in a quicker cadence. The parameter change expands the basin of attraction of the walking gait and leads to a fast, compact walking pattern.

## Gamma



Increasing the slope inclination to  $\gamma = 0.1$  rad reduces the critical threshold to  $\omega_1 \approx 0.913$  rad/s, just below the fixed  $\dot{\theta}_0 = 0.95$  rad/s. As expected, the system quickly converges to a stable walking gait. The phase portrait shows a rapid spiral onto a new limit cycle. This cycle differs from the default case: it exhibits a higher peak velocity (1.7 rad/s) and an asymmetric shape, reflecting the shifted equilibrium position due to the steeper slope. The system thus benefits from increased gravitational energy, enabling a faster and more energetic gait.

## Conclusion on System Parameter Modifications

This analysis demonstrates that modifications to the rimless wheel's physical parameters have a profound impact on its dynamic behavior, directly addressing the guiding questions of the exercise.



## How do parameter changes affect the equilibrium conditions?

All three parameter changes—increasing leg length ( $l$ ), decreasing the inter-leg angle ( $\alpha$ ), and increasing the slope inclination ( $\gamma$ )—were shown to fundamentally affect the system’s equilibrium conditions. While the static equilibrium point and the walking limit cycle remain the two primary attractors, the modifications successfully **altered the boundaries of their respective basins of attraction**.

Each change was specifically chosen to lower the critical energy threshold required for walking. As a result, an initial condition ( $\dot{\theta}_0 = 0.95$  rad/s) that previously belonged to the basin of attraction of the static equilibrium was successfully brought into the basin of attraction of the stable limit cycle. This confirms that the system’s propensity to walk or halt is not only a function of its initial state but is critically dependent on its physical design and environment.

## Do these modifications result in different limit cycles?

Yes, each modification resulted in a **new and distinct limit cycle**, demonstrating that there is no single ”walking gait” for the rimless wheel. Instead, the characteristics of the stable periodic motion are a direct consequence of the system’s parameters:

- **Increasing leg length ( $l$ )** resulted in a limit cycle with a lower peak velocity and a slower cadence, corresponding to a more deliberate, long-legged stride.
- **Decreasing the inter-leg angle ( $\alpha$ )** produced a limit cycle with a significantly reduced angular range but a higher peak velocity, corresponding to a faster gait with short, quick steps.
- **Increasing the slope inclination ( $\gamma$ )** led to a more energetic limit cycle with a higher peak velocity, reflecting the increased energy input from gravity at each step.

In conclusion, modifying the physical parameters of the rimless wheel does not merely enable or disable walking; it fundamentally redefines the nature of the stable gait itself. Each parameter set gives rise to a unique limit cycle with its own characteristic speed, cadence, and shape in the phase space.